RESEARCH ARTICLE

Voltage Control of IPMSM Servo Drive in Constant Power Region With Intelligent Parameter Estimation

FAA-JENG LIN, (Fellow, IEEE), **CHIH-WEI LIU, AND PO-LUN WANG**
Department of Electrical Engineering, National Central University, Chungli 320, Taiwan

Corresponding author: Faa-Jeng Lin (linfj@ee.ncu.edu.tw)

ABSTRACT A novel voltage control scheme for an interior permanent magnet synchronous motor (IPMSM) servo drive in the constant power region with intelligent estimation of the motor parameter is proposed in this study. In the novel voltage control scheme, a feedforward voltage angle controller is proposed where an intelligent parameter estimation method by using a wavelet fuzzy neural network (WFNN) is developed to estimate the q-axis inductance online. In this study, in order to minimize the copper loss, a flux-weakening (FW) control scheme under maximum phase voltage is developed first. Then, an adaptive backstepping based nonlinear controller (ABNC) considering nonzero d-axis current is developed to improve the robustness of the speed control. The Lyapunov stability theorem is used to derive the adaptive law of the online estimation of the lumped uncertainty to ensure the asymptotical stability of the ABNC. Moreover, a feedforward voltage angle controller is developed for the voltage control where the q-axis current controller is retained in order to ensure the steady-state performance of the control system. Furthermore, the WFNN is adopted to estimate the actual q-axis inductance value online for the feedforward voltage angle controller to improve the dynamic response. In addition, some experimental results are demonstrated to verify the effectiveness of the proposed voltage control scheme with ABNC in the constant power region.

INDEX TERMS Interior permanent magnet synchronous motor (IPMSM), adaptive backstepping based nonlinear controller (ABNC), maximum torque per ampere (MTPA) control, flux-weakening (FW) control, online parameter estimation, wavelet fuzzy neural network (WFNN).

I. INTRODUCTION

There are many attractive characteristics of the interior permanent magnet synchronous motors (IPMSMs) including wide speed operating range, superior power density, high efficiency, and high torque-to-inertia ratio. These features permit the IPMSMs to be operated not only in the constant torque region but also in the constant power region up to a high speed by using flux weakening. Thus, IPMSMs has been adopted in many industrial applications [1], [2], [3], [4]. Moreover, to improve the control performance and efficiency of the IPMSM servo drives, optimal control methods such as maximum torque per ampere (MTPA) control and

flux-weakening (FW) control have been proposed [1], [2], [3], [4]. In order to utilize the advantages of the reluctance torque term of the IPMSMs in the constant torque region, the MTPA control has been developed to improve the torque output. Furthermore, the FW control is an important issue in the range of high speed with the back electromotive force (EMF) increasing along with the rising speed, which will reach the limit of dc-link voltage in the constant power region.

There are mainly two strategies to achieve the FW control which are the current control methods [4], [5], [6], the voltage control methods [7], [8], [9], [10], [11]. In [4], to limit the inverter output voltage to the maximum phase voltage of the inverter at high speed, a voltage control loop was designed for the current control in the constant power region. A FW control was achieved by using current control with the flux level

being adjusted automatically by the outer voltage regulation loop to prevent saturation of the current regulator in [5]. In [6], an improved FW control algorithm of IPMSMs based on torque feedforward technique was proposed to generate large and stable torque in the FW region. Moreover, traditional FW control using current control methods, which are developed from the vector control methods, usually adopt two proportional-integral (PI) regulators to control the d-axis and the q-axis current separately. However, the stability of the control system of traditional FW control may be affected by the undesired current saturation phenomenon. Though many anti-windup strategies for the permanent magnet synchronous motors (PMSMs) were presented in the literature [6], the conflict between the two current regulators still lead to the slow dynamic response or even the instability of the control system in high speed [5]. On the other hand, the voltage control methods can make fully use of dc-link voltage and eliminate the conflict between the two current regulators [7], [8], [9], [10], [11]. In [7], a novel torque control based on voltage phase angle control was proposed to provide more accurate torque for the IPMSMs in the constant power region. A voltage angle based FW control scheme appropriate for the operation of surface PMSMs over a wide range of speed was proposed in [8]. A single current regulator which controls the d-axis current actively with a fixed q-axis voltage command was proposed in [9]. In [10], a single q-axis current regulator with variable voltage angle control method was proposed. In [11], a voltage control scheme was developed to control the torque with the voltage angle in the FW region when the inverter output voltage amplitude is saturated. Furthermore, an online stator flux estimation method was proposed in [12], in which a real-time torque control was proposed to satisfy both torque control accuracy and high-efficiency operation in consideration of flux linkage variations in both the MTPA and FW regions. Both stator flux linkages and dynamic inductances are estimated online in [12] to consider the flux variations in real time.

Although the control performance and dynamic response of the IPMSMs are excellent, the motor parameters are easily varying at different operating conditions. Therefore, the development of parameters estimation of IPMSMs has been a popular research topic in the past two decades [13], [14], [15], [16], [17], [18]. In [13], an online parameter estimation method based on a discrete-time dynamic model for the IPMSMs was proposed. The proposed method consists of two affine projection algorithms and has adopted the difference in dynamics of motor parameters. Moreover, an estimation method of the spatial inductance map by spatially scanning the motor using the sinusoidal voltage injection was developed in [14]. In [15], a real-time method to estimate the inductances of an IPMSM by using the measured dc-link voltage of the inverter and the derivatives of the stator currents at certain voltage vectors during each pulse width modulation cycle was proposed. Furthermore, an adaptive online parameter estimation method for the high-speed control of an IPMSM drive was developed in [16]. In [17], the Adaline

NN algorithm was employed to design the estimators for the rotor flux linkage and stator winding resistance. In addition, an online parameter estimation methodology using d-axis current injection, which can estimate the distortion voltage of the current-controlled voltage source inverter (CCVSI), the varying dq-axis inductances, and the rotor flux, was proposed in [18]. However, most of the parameter estimation methods mentioned above were only developed for the control of the IPMSMs in the constant torque region.

The PI speed controller is largely adopted in many control applications due to its simplicity. Nevertheless, the disadvantages of the PI controller, such as sensitive to parameter variations and external disturbances, is well known. On the other hand, the backstepping control, as a systematic and nonlinear recursive design method, has attracted much attention for the nonlinear feedback control [19], [20], [21], [22], [23]. Moreover, the backstepping control is based on Lyapunov stability theory. Its control law is derived by constructing the Lyapunov function, and the global asymptotic stability is ensured. However, the sign function in the backstepping control may cause undesired chattering phenomena. Therefore, to reduce the chattering phenomena and improve the control performance, some control methods such as adaptive control [19], [20], intelligent control [21], and sliding mode control [22], [23], have been proposed to merge with the backstepping control. Therefore, one of the objectives of this study is to replace the conventional PI speed controller by an adaptive backstepping based nonlinear controller (ABNC).

To improve the control performance of an IPMSM servo drive in the constant power region, a novel voltage control scheme with a feedforward voltage angle controller is developed in this study. Moreover, an intelligent parameter estimation method by using a wavelet fuzzy neural network (WFNN) [24], [25], [26] is proposed to estimate the q-axis inductance online for the feedforward voltage angle controller. This study is organized into six sections. The dynamic analysis of a field-oriented control (FOC) IPMSM servo drive with traditional FW control is studied in Sec. II. Then, an ABNC speed controller considering nonzero d-axis current with adaptive online estimation of the lumped uncertainty is discussed in Sec. III. Furthermore, the proposed voltage control by using a feedforward voltage angle control with the q-axis current controller is introduced in Sec. IV. In addition, the experimentation based on a TMS320F28075 32-bit floating-point digital signal processor (DSP) with some experimental results to verify the effectiveness of the proposed voltage control scheme is presented in Sec. V. Finally, some conclusions are addressed in Sec. VI.

The main contributions of this study are listed as follows: (1) An ABNC speed controller considering nonzero d-axis current is proposed to improve the robustness of the speed control. (2) A feedforward voltage angle controller, in which an intelligent parameter estimation method using WFNN is adopted to estimate the q-axis inductance online, is developed. (3) The current control and voltage control modes with ABNC speed controller to achieve the current and voltage

control of an IPMSM servo drive at different speeds and load torque conditions are successfully implemented.

II. TRADITION FW CONTROL OF IPMSM

The voltage model at steady state of an IPMSM in the *dq* reference frame can be expressed as follows:

$$v_d = r_s i_d - \omega_e L_q i_q \tag{1}$$
$$v_q = r_s i_q + \omega_e (L_d i_d + \lambda_m) \tag{2}$$

where v_d and v_q are the *d*-axis and *q*-axis voltages; i_d and i_q are the *d*-axis and *q*-axis currents; r_s is the stator resistance; L_d and L_q are the *d*-axis and *q*-axis inductances; λ_m is the permanent-magnet (PM) flux of the rotor; ω_e is the electrical speed. Moreover, voltage-fed inverters are widely used in the IPMSM servo drive system. The maximal phase voltage limit V_{s_max} of the inverter is defined by the dc-link voltage v_{dc}, which equals to $v_{dc}/\sqrt{3}$, for the space vector pulse width modulation (SVPWM). Furthermore, the current limit i_{s_max} is defined by the machine rated current i_{rated}. The following two constraints must be fulfilled for the control of an IPMSM:

$$v_d^2 + v_q^2 = v_s^2 \leq v_{s\_max}^2 \tag{3}$$
$$i_d^2 + i_q^2 = i_s^2 \leq i_{s\_max}^2 = (\sqrt{2}\,i_{rated})^2 \tag{4}$$

For the speeds above the rated speed, where the stator resistance can be neglected, (1) and (2) can be simplified as follows:

$$v_d = -\omega_e L_q i_q \tag{5}$$
$$v_q = \omega_e L_d i_d + \omega_e \lambda_m \tag{6}$$

Combining (3), (5) and (6), the voltage limit ellipse of an IPMSM can be obtained as follows:

$$\frac{(i_d + \frac{\lambda_m}{L_d})^2}{(\frac{V_{s\_max}}{\omega_e L_d})^2} + \frac{i_q^2}{(\frac{V_{s\_max}}{\omega_e L_q})^2} = 1 \tag{7}$$

According to (4) and (7), the operation limit of IPMSM with the current limit circle and voltage limit ellipses in *dq*-axis current plane with four different electrical speeds and electromagnetic torques are shown in Fig. 1 where T_e is the electromagnetic torque. In addition, the MTPA curve is obtained by using (26) and will be discussed in Sec. IV. In the constant torque region, the operating points are located on the MTPA curve for minimizing the copper loss. Additionally, the overlapping between the current limit circle and voltage limit ellipse defines the FW operating region. The operating region becomes smaller along with the shrinking of the voltage limit ellipse when the electrical speed increases [6], [11].

Fig. 2 is the block diagram of an FOC IPMSM servo drive by using the SVPWM CCVSI with the conventional MTPA and FW control. In Fig. 2, first, the actual rotor position θ_{rm} of the motor is determined by the encoder, and the mechanical speed ω_{rm} is obtained by differentiating θ_{rm}. The electrical angle θ_{re} can be obtained by multiplying θ_{rm} with the pole pairs $P/2$. Next, the mechanical speed ω_{rm} is subtracted from
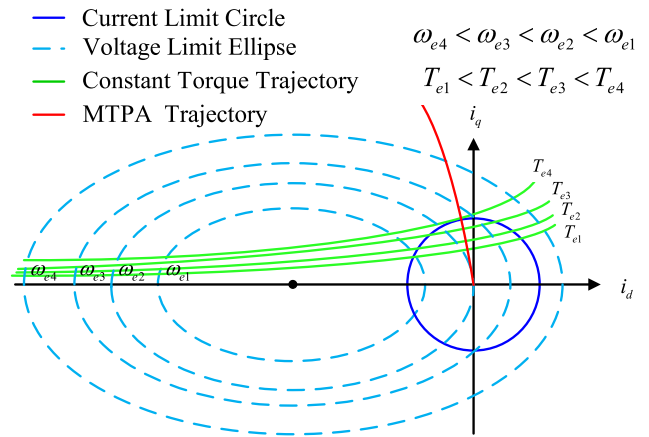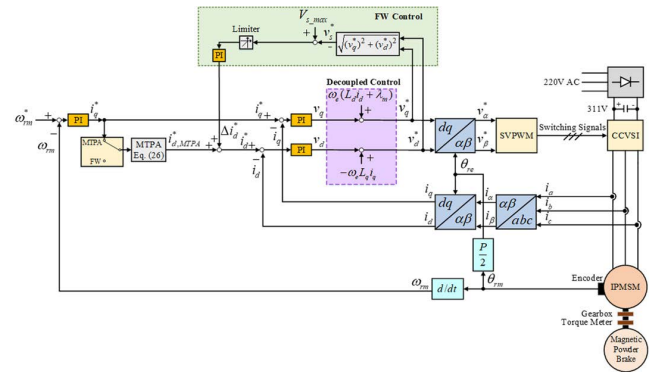

FIGURE 1. Operation limits of IPMSM.

FIGURE 2. Block diagram of IPMSM servo drive with conventional MTPA and FW control.

the mechanical speed command ω_{rm}^* to obtain the mechanical speed error e_1. Then, e_1 is inputted into PI speed controller to get the *q*-axis current command i_q^*. Moreover, i_q^* is substituted into the MTPA formula to derive the *d*-axis current command $i_{d,MTPA}^*$ for the MTPA control. While the FW control is proceeded, the motor speed will be increased above the rated speed. The input of the MTPA block shown in Fig. 2 will be switched to FW and the $i_{d,MTPA}^*$ will be kept constant during the FW control. Furthermore, to make sure that the stator voltage command v_s^* will not exceed the phase voltage limit V_{s_max} of the inverter, $V_{s\_max} - v_s^*$ is inputted into a PI controller to generate the variation of *d*-axis current command Δi_d^* which is a negative value. Only when the inverter output voltage v_s^* exceeds the maximum phase voltage V_{s_max} of the inverter, the input of the PI controller will be nonzero. As shown in Fig. 2, the three-phase currents i_a, i_b and i_c of the CCVSI are transformed to the corresponding *q*-axis current i_q and *d*-axis current i_d by using the coordinate transformation. In addition, i_q and i_d are subtracted respectively from i_q^* and i_d^*, and then the *dq*-axis voltage commands v_d^* and v_q^* are obtained through the PI controllers of the current loop with the decouple control shown in Fig. 2. After v_d^* and v_q^* are obtained, v_α^* and v_β^* are derived by using coordinate transformation. Additionally, the switching signals of the insulated-gate bipolar transistors (IGBTs) of the CCVSI are generated
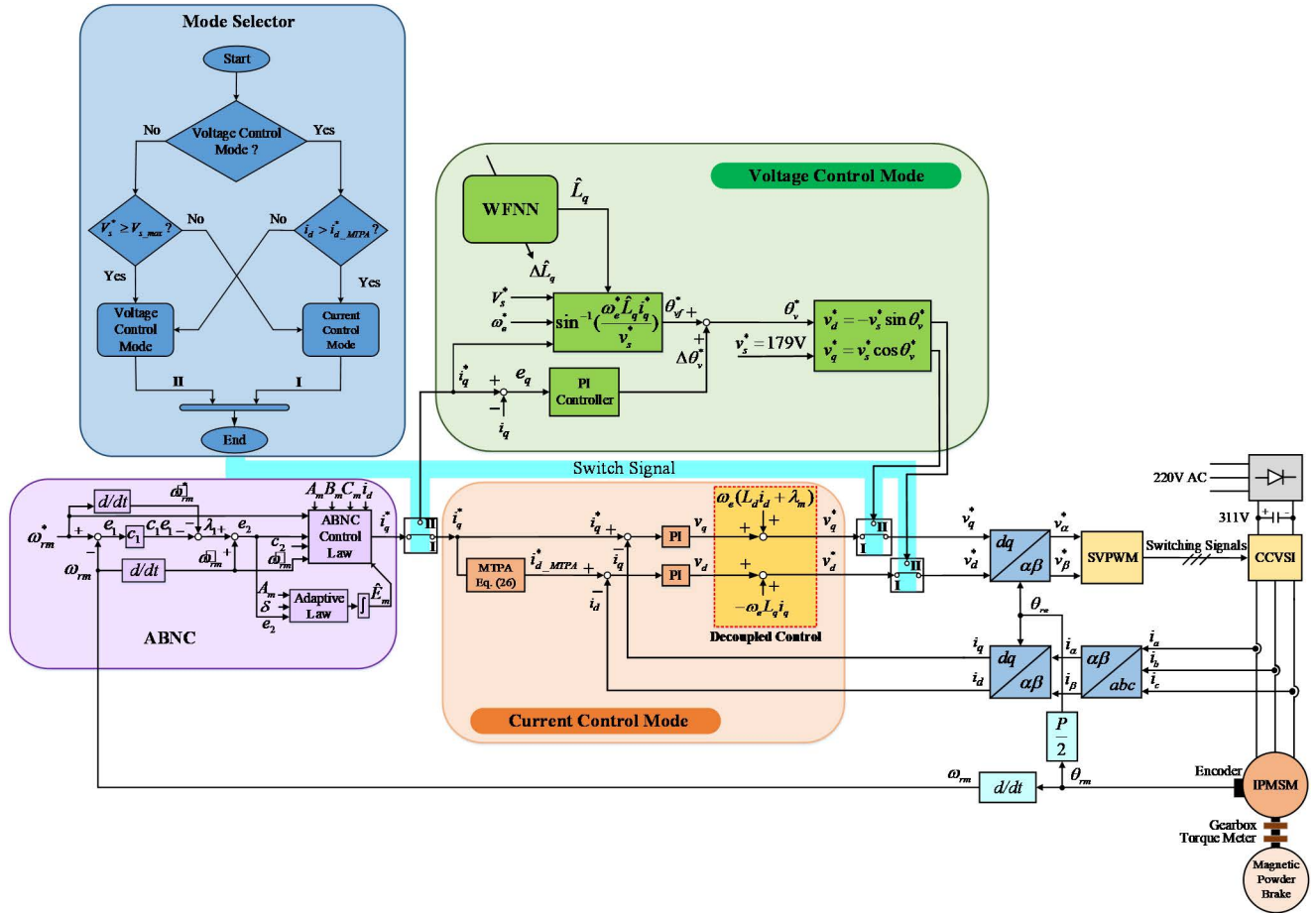
FIGURE 3. Block diagram of proposed voltage control IPMSM servo drive with ABNC.

through SVPWM. Finally, the switching signals are sent to the IGBTs to achieve the conventional MTPA and FW control. However, when the IPMSM servo drive is operated above the rated speed, the undesired current saturation phenomenon caused by the integrator windup problem of the PI current controllers is the main disadvantage of the conventional FW control system.

III. ADAPTIVE BACKSTEPPING BASED NONLINEAR CONTROLLER

Fig. 3 is the block diagram of the proposed voltage control IPMSM servo drive where the ABNC is adopted as the speed controller. In Fig. 3, first, e_1 is inputted into the ABNC to get the q-axis current command, and i_q^* is substituted into the MTPA formula to derive the d-axis current command $i_{d\_MTPA}^*$ for the MTPA control in the constant torque region. While the FW control is proceeded, the motor speed will be increased above the rated speed. As the stator voltage command reaches the maximum phase voltage V_{s_max}, the mode selector shown in Fig. 3 will be switched to the voltage control mode for the constant power region. Moreover, the WFNN is adopted to estimate the correct q-axis inductance value $\hat{L}_q$ online. The

$\hat{L}_q$ is used to obtain the feedforward voltage angle command θ_{vf}^* as shown in the block of voltage control mode of Fig. 3. Furthermore, the q-axis current error e_q is inputted into PI controller to generate the compensating value of voltage angle $\Delta\theta_v^*$. Owing to the voltage magnitude is fixed in voltage control mode, the dq-axis voltage commands can be obtained from the voltage angle command θ_v^*.

The mechanical dynamic equation of the IPMSM servo drive system can be represented as follows:

$$T_e = J\dot{\omega}_{rm} + B\omega_{rm} + T_L \qquad (8)$$

where J is the inertia coefficient; B is the damping coefficient; T_L is the load torque. By neglecting the load torque, (8) can be modified as

$$\dot{\omega}_{rm} = -\frac{B}{J}\omega_{rm} + \frac{T_e}{J} \qquad (9)$$

The developed electromagnetic torque T_e can be represented by the following equation:

$$T_e = \frac{3}{2}\frac{P}{2}[\lambda_m i_q + (L_d - L_q)i_d i_q] \qquad (10)$$

The IPMSM servo drive system can be formulated by rewriting (9) and (10) as follows:

$$\dot{\omega}_{rm} = -\frac{\bar{B}}{\bar{J}}\omega_{rm} + \frac{3P\bar{\lambda}_m}{4\bar{J}}i_q^* + \frac{3P(\bar{L}_d - \bar{L}_q)}{4\bar{J}}i_d i_q^*$$
$$= A_m\omega_{rm} + B_m i_q^* + C_m i_d i_q^* \qquad (11)$$

where $A_m = -\frac{\bar{B}}{\bar{J}}$; $B_m = \frac{3P\bar{\lambda}_m}{4\bar{J}}$; $C_m = \frac{3P(\bar{L}_d - \bar{L}_q)}{4\bar{J}}$; $\bar{B}$, $\bar{J}$, $\bar{\lambda}_m$, $\bar{L}_d$ and $\bar{L}_q$ are the nominal values of damping coefficient, moment of inertia, PM flux, d-axis inductance and q-axis inductance, respectively. By considering the uncertainties including the existence of parameter variations and external disturbances of the IPMSM servo drive system, (11) can be rewritten as

$$\dot{\omega}_{rm} = (A_m + \Delta A_m)\omega_{rm} + (B_m + \Delta B_m)i_q^*$$
$$+ (C_m + \Delta C_m)i_d i_q^* + (D_m + \Delta D_m)T_L$$
$$= A_m\omega_{rm} + B_m i_q^* + C_m i_d i_q^* + E_m \qquad (12)$$

where $D_m = -\frac{1}{J}$; ΔA_m, ΔB_m, ΔC_m and ΔD_m are the time-varying parameter variations. Then, E_m is named the lumped uncertainty and defined as follows:

$$E_m = \Delta A_m\omega_{rm} + \Delta B_m i_q^* + \Delta C_m i_d i_q^* + (D_m + \Delta D_m)T_L \qquad (13)$$

And E_m is assumed to be bounded

$$|E_m| \leq \rho \qquad (14)$$

where ρ is a given positive constant.

Define the speed tracking error and its derivative term as follows:

$$e_1 = \omega_{rm}^* - \omega_{rm} \qquad (15)$$
$$\dot{e}_1 = \dot{\omega}_{rm}^* - \dot{\omega}_{rm} \qquad (16)$$

where $\dot{\omega}_{rm}$ can be viewed as a virtual control input. Then, define the following stabilizing function as:

$$\lambda_1 = -c_1 e_1 - \dot{\omega}_{rm}^* \qquad (17)$$

where λ_1 is a positive constant. Moreover, a virtual control error is defined as:

$$e_2 = \dot{\omega}_{rm} + \lambda_1 = \dot{\omega}_{rm} - c_1 e_1 - \dot{\omega}_{rm}^* \qquad (18)$$

Furthermore, a Lyapunov function is chosen as follows:

$$V = \frac{1}{2}e_1^2 + \frac{1}{2\delta}|\tilde{E}_m|^2 > 0 \qquad (19)$$

where V is a positive definite function; $\tilde{E}_m = E_m - \hat{E}_m$ and $\hat{E}_m$ is the estimated value of E_m; δ is a positive constant. Taking the time derivative of the Lyapunov function and using (12) and (18), one can obtain:

$$\dot{V} = e_1\dot{e}_1 + \frac{1}{\delta}\tilde{E}\dot{\tilde{E}} = e_1(\dot{\omega}_{rm}^* - \dot{\omega}_{rm}) - \frac{1}{\delta}\tilde{E}_m\dot{\hat{E}}_m$$
$$= e_1(-c_1 e_1 - e_2) - \frac{1}{\delta}\tilde{E}_m\dot{\hat{E}}_m$$

$$= -c_1 e_1^2 - (\omega_{rm}^* - \omega_{rm})e_2 - \frac{1}{\delta}\tilde{E}_m\dot{\hat{E}}_m$$

$$= -c_1 e_1^2 - [\omega_{rm}^* - (\frac{1}{A_m})(\dot{\omega}_{rm} - B_m i_q^* - C_m i_d i_q^* - E_m)]$$
$$\times e_2 - \frac{1}{\delta}\tilde{E}_m\dot{\hat{E}}_m$$

$$= -c_1 e_1^2 - [\omega_{rm}^* - \frac{\dot{\omega}_{rm}}{A_m} + (\frac{1}{A_m})(B_m + C_m i_d)i_q^*]$$
$$\times e_2 - \frac{e_2}{A_m}(\tilde{E}_m + \hat{E}_m) - \frac{1}{\delta}\tilde{E}_m\dot{\hat{E}}_m$$

$$= -c_1 e_1^2 - [\omega_{rm}^* - \frac{\dot{\omega}_{rm}}{A_m} + (\frac{1}{A_m})(B_m + C_m i_d)i_q^* + \frac{1}{A_m}\hat{E}_m]$$
$$\times e_2 - \frac{e_2}{A_m}\tilde{E}_m - \frac{1}{\delta}\tilde{E}_m\dot{\hat{E}}_m$$

$$= -c_1 e_1^2 - [\omega_{rm}^* - \frac{\dot{\omega}_{rm}}{A_m} + (\frac{1}{A_m})(B_m + C_m i_d)i_q^*$$
$$+ \frac{1}{A_m}\hat{E}_m]e_2 - \frac{\tilde{E}_m}{\delta}(\frac{\delta e_2}{A_m} + \dot{\hat{E}}_m) \qquad (20)$$

Therefore, according to (20), the ABNC control law U_{ABNC} and adaptive law $\dot{\hat{E}}_m$ are designed as follows:

$$U_{ABNC} = i_q^* = \frac{1}{B_m + C_m i_d}(\dot{\omega}_{rm} - A_m\omega_{rm}^* - \hat{E}_m + A_m c_2 e_2) \qquad (21)$$

$$\dot{\hat{E}}_m = -\frac{\delta}{A_m}e_2 \qquad (22)$$

Substituting (21) and (22) into (20), the following equation can be obtained:

$$\dot{V} = -c_1 e_1^2 - c_2 e_2^2 \leq 0 \qquad (23)$$

Since $\dot{V}(t) \leq 0$ is negative semidefinite and $V(t) > 0$, it implies that e_1, e_2, and $\tilde{E}_m$ are nonincreasing and bounded. According to Lyapunov Theorem and Barbalat's Lemma, e_1 and e_2 will converge to zero as $t \to \infty$. Thus, considering the dynamic equation of the IPMSM servo drive system represented by (12), if the ABNC control law and adaptive law are designed as (21) and (22), the asymptotically stable of the IPMSM servo drive system using the ABNC speed controller can be guaranteed.

IV. NOVEL VOLTAGE CONTROL SCHEME OF IPMSM

To achieve wide speed range operation, two control modes are proposed for the IPMSM servo drive and the switch signal is obtained by using the mode selector as shown in Fig. 3. In the current control mode, the switching signal of the mode selector turns to the voltage control mode when the stator voltage command reaches the maximum phase voltage ($V_{s\_max} \approx 179V$) of the CCVSI. On the other hand, in the voltage control mode, the switching signal of the mode selector turns to the current control mode when the d-axis current i_d is larger than d-axis current command of MTPA $i_{d,MTPA}^*$. The above description can be summarized as:

$v_s^* \geq V_{s\_max}$:

Current Control Mode $\to$ Voltage Control mode
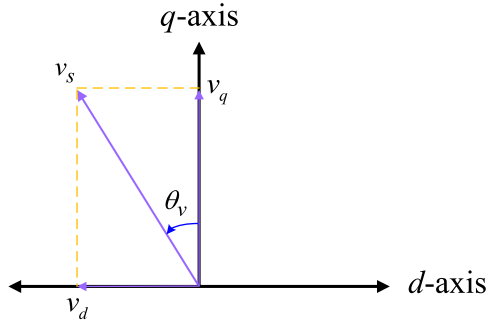
(24)

FIGURE 4. *dq*-axis voltage coordinate of IPMSM.

$i_d > i^*_{d,MTPA}$:

     Voltage Control Mode $\rightarrow$ Current Control Mode

$$\tag{25}$$

A. CURRENT CONTROL MODE

In the current control mode, in order to maximize the motor efficiency, the MTPA method is used to minimize the copper loss. According to MTPA formula, the *d*-axis current command $i^*_{d,MTPA}$ can be obtained as follows [4]:

$$i^*_{d,MTPA} = \frac{-\lambda_m + \sqrt{\lambda_m^2 + 4(L_d - L_q)^2 i_q^{*2}}}{2(L_d - L_q)} \tag{26}$$

B. VOLTAGE CONTROL MODE

When the IPMSM servo drive is operated above the rated speed and the stator voltage command reaches the maximum phase voltage, the voltage control mode is adopted. Since the inductances of the IPMSM vary nonlinearly with different operating conditions, a novel voltage control scheme is proposed in Fig. 3. In the voltage control mode, the magnitude of stator voltage command is fixed, that is $v^*_s = V_{s\_max}$, which is 179V. According to the *dq*-axis voltage coordinate of IPMSM shown in Fig. 4, the *d*-axis and *q*-axis voltage commands can be expressed as:

$$v^*_d = -v^*_s \sin\theta^*_v \tag{27}$$
$$v^*_q = v^*_s \cos\theta^*_v \tag{28}$$
$$(v^*_d)^2 + (v^*_q)^2 = (V_{s\_max})^2 \tag{29}$$

Based on formula (21), (22) and (27), the feedforward voltage angle command is designed as:

$$\theta^*_{vf} = \sin^{-1}\left(\frac{\omega^*_e \hat{L}_q i^*_q}{v^*_s}\right) \tag{30}$$

where ω^*_e is the command of the electrical speed and can be obtained by multiplying ω^*_{rm} with the pole pairs *P*/2. Considering the steady state stability of the proposed control system, the *q*-axis current regulator is still retained. Besides, *q*-axis current error can be represented as:

$$e_q = i^*_q - i_q \tag{31}$$

A PI controller is adopted to generate the compensating value of voltage angle $\Delta\theta^*_v$ by using e_q. Then, the voltage angle command can be expressed as:

$$\theta^*_v = \theta^*_{vf} + \Delta\theta^*_v \tag{32}$$

However, since the *q*-axis inductance value $\hat{L}_q$ shown in (30) varies significantly in FW region, a WFNN [24], [25], [26] is adopted to estimate the *q*-axis inductance value $\hat{L}_q$ online as shown in Fig. 3 to improve the dynamic response of voltage control.

C. ESTIMATION OF DISTORTION VOLTAGE

Owing to the nonlinearity and time delay of the CCVSI, the distortion voltage errors between the *dq*-axis voltages command and the real *dq*-axis voltages of the IPMSM servo drive are inevitable. Thus, considering the distortion voltage errors, the *dq*-axis voltages command can be expressed as follows in the FW operating region:

$$v^*_d = -\omega_e L_q i_q + D_d V_{dead} \tag{33}$$
$$v^*_q = \omega_e L_d i_d + \omega_e \lambda_m + D_q V_{dead} \tag{34}$$

where V_{dead} is the distortion voltage and D_d, D_q are the distorted coefficients [18]. To estimate the distortion voltage V_{dead}, the instantaneous measurement of the electrical speed, *dq*-axis voltages and currents are required. However, when the motor is operated at high speed, these signals will be contaminated by various noises. Therefore, the smoothing values of the measured signals are adopted to improve the estimation accuracy. Eq. (33), (34) can be rewritten as follows:

$$\bar{v}^*_d = -\bar{\omega}_e L_q \bar{i}_q + \bar{D}_d V_{dead} \tag{35}$$
$$\bar{v}^*_q = \bar{\omega}_e L_d \bar{i}_d + \bar{\omega}_e \lambda_m + \bar{D}_q V_{dead} \tag{36}$$

where the smoothing values of *dq*-axis voltage commands $\bar{v}^*_{dq}$, *dq*-axis current $\bar{i}_{dq}$ and electrical speed $\bar{\omega}_e$ are averaged every ten times. Moreover, the smoothing values of distorted coefficients $\bar{D}_d$, $\bar{D}_q$ are defined as follows [18]:

$$\bar{D}_d = \frac{1}{N}\sum_{k=1}^{N} 2\sin[\theta_{rmk} - int\{\frac{3(\theta_{rmk} + \gamma + \frac{\pi}{6})}{\pi}\} \times \frac{\pi}{3}]$$

$$\tag{37}$$

$$\bar{D}_q = \frac{1}{N}\sum_{k=1}^{N} 2\cos[\theta_{rmk} - int\{\frac{3(\theta_{rmk} + \gamma + \frac{\pi}{6})}{\pi}\} \times \frac{\pi}{3}]$$

$$\tag{38}$$

where $N = 360$ for 360 degrees; γ is the current angle; θ_{rmk} is the k_{th} rotor angle. Besides, $\bar{D}_d$ and $\bar{D}_q$ are only functions of the current angle and are independent of rotor position. Since the calculation of the smooth values needs to substitute and accumulate the rotor angle 360 times according to different current angles, it will take a large amount of calculation and is impossible to obtain the smooth values of the distortion coefficients in one interrupt sampling time. For
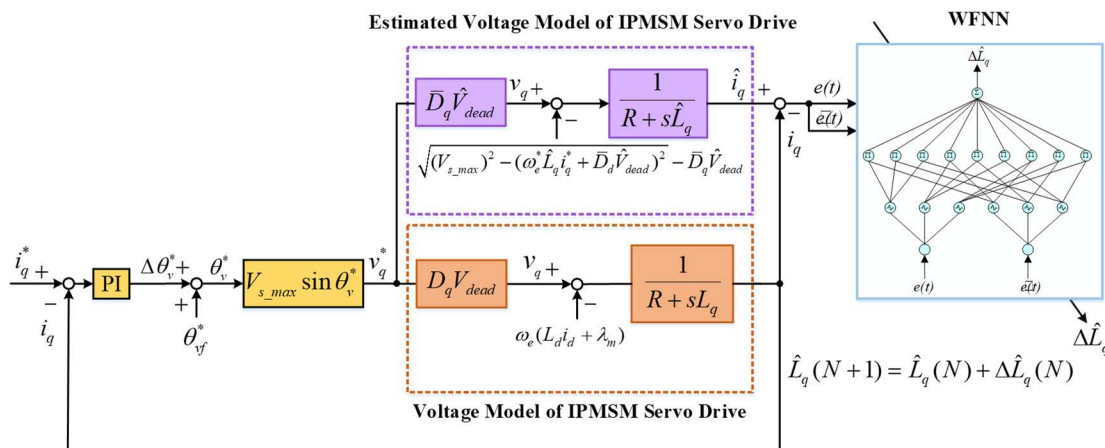
FIGURE 5. Block diagram of *q*-axis inductance estimation.

the convenience of calculation in real time, the curve fitting is adopted to equate the distorted coefficients as follows:

$$\bar{D}_d \approx 1.91 \sin(\gamma + 3.132) \tag{39}$$
$$\bar{D}_q \approx 1.91 \sin(\gamma + 1.561) \tag{40}$$

Furthermore, the following equation can be obtained by multiplying (35) by i_d and multiplying (36) by i_q and adding together:

$$\bar{V}_d^* \bar{i}_d + \bar{V}_q^* \bar{i}_q = \bar{\omega}_e[(L_d - L_q)\bar{i}_q\bar{i}_d + \lambda_m \bar{i}_q] + \hat{V}_{dead}(\bar{D}_d \bar{i}_d + \bar{D}_q \bar{i}_q) \tag{41}$$

In addition, substituting $[(L_d - L_q)\bar{i}_q\bar{i}_d + \lambda_m \bar{i}_q] = T_e \times \frac{4}{3P} = \frac{T_e}{6}$ to (41) with $P = 8$ results in the following equation:

$$\bar{V}_d^* \bar{i}_d + \bar{V}_q^* \bar{i}_q = \bar{\omega}_e \frac{T_e}{6} + \hat{V}_{dead}(\bar{D}_d \bar{i}_d + \bar{D}_q \bar{i}_q) \tag{42}$$

Thus, the distortion voltage V_{dead} can be estimated as follows:

$$\hat{V}_{dead} = \frac{\bar{V}_d^* \bar{i}_d + \bar{V}_q^* \bar{i}_q - \bar{\omega}_e \frac{T_e}{6}}{(\bar{D}_d \bar{i}_d + \bar{D}_q \bar{i}_q)} \tag{43}$$

where $\hat{V}_{dead}$ is the estimated value of V_{dead}.

D. ONLINE ESTIMATION OF Q-AXIS INDUCTANCE

The block diagram using the intelligent parameter estimation method to estimate the *q*-axis inductance $\hat{L}_q$ is shown in Fig. 5. There are two mostly adopted neuron networks, the fuzzy neural network (FNN) and the wavelet neural network (WNN), in the intelligent control systems. The FNN possesses the characteristic of fuzzy reasoning in handling uncertain information and the characteristic of artificial neural networks in learning from processes. Moreover, the WNN with reduced network size has the ability of converging quickly with high precision owing to the time–frequency localization properties of wavelets. Since the WFNN combines the aforementioned advantages of the FNN and WNN [24], [25], [26], the *q*-axis inductance is estimated by the

WFNN as shown in Fig. 5. The *q*-axis current i_q obtained from the IPMSM servo drive, i.e. the voltage model of the IPMSM servo drive, is subtracted from the estimated *q*-axis current $\hat{i}_q$ of the estimated voltage model of the IPMSM servo drive to obtain the error e. Then, e and its derivative $\dot{e}$ are inputted into the WFNN to obtain the adaptation value of the *q*-axis inductance $\Delta \hat{L}_q$ online.

The coupling terms of both the real and estimated *q*-axis voltage model are required as shown in Fig. 5. Therefore, after some mathematical manipulations using (3), (33) and (34), one can obtain:

$$\omega_e(L_d i_d + \lambda_m) = \sqrt{(v_{s\_max})^2 - (-\omega_e L_q i_q + D_d V_{dead})^2} - D_q V_{dead} \tag{44}$$

Substituting $\bar{D}_d, \bar{D}_q, \hat{V}_{dead}, \omega_e^*$ and i_q^* into (44), the coupling term of the estimated voltage model can be expressed as:

$$\omega_e(L_d i_d + \lambda_m) = \sqrt{(v_{s\_max})^2 - (-\omega_e^* \hat{L}_q i_q^* + \bar{D}_d \hat{V}_{dead})^2} - \bar{D}_q \hat{V}_{dead} \tag{45}$$

Moreover, the output of the WFNN is the adaptation value of the *q*-axis inductance $\Delta \hat{L}_q$. Thus, the estimated value of the *q*-axis inductance can be obtained by using the following equation:

$$\hat{L}_q(N + 1) = \hat{L}_q(N) + \Delta \hat{L}_q(N) \tag{46}$$

The adaptation is processed recursively until $\hat{i}_q = i_q$, which is the same as the traditional model following control scheme. Then, the steady-state estimation value of the *q*-axis inductance $\hat{L}_q$ at a specific high-speed operating condition can be obtained. Furthermore, since the coupling term shown in (45) is replaced by the right hand side of the equality, the variations of L_d and λ_m are effectively taken into account during the adjustment of the *q*-axis inductance.

V. EXPERIMENTATION
The experimental setup of the IPMSM servo drive system are shown in Fig. 6. The IPMSM test platform is composed
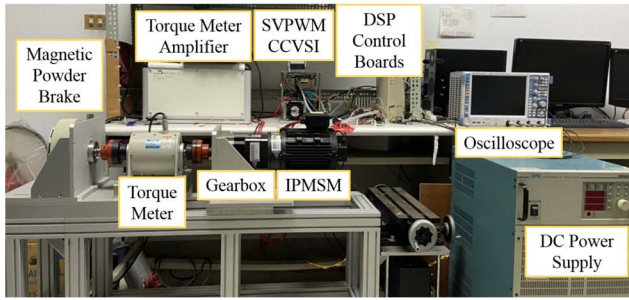
FIGURE 6. Photo of experimental setup.

TABLE 1. Parameters of magnetic powder brake and IPMSM.

	Items	Units	Quantities
Magnetic Powder Brake	Torque	Nm	50
	Rated current	A	2.15
	Coil resistance	Ohm	11.14
	Mass of powder	g	60
	Maximum rotating speed	rpm	1800
IPMSM	Pole number		8
	Rated power	W	2000
	Rated line voltage	V	220
	Rated current	A	10.6
	Rated torque	Nm	9.5
	Rated speed	rpm	2000
	d-axis inductance	mH	3.48
	q-axis inductance	mH	6.16
	Magnetic flux	Wb	0.143
	Resistance	Ohm	0.57
	Viscous damping	Nm/(rad/sec)	2.69×10^{-3}
	Inertia	Nm/(rad/sec^2)	4.07473×10^{-3}

FIGURE 7. Torque-Speed Curve and four experimental cases.

of an IPMSM, a gearbox (with gear ratio 4:1), a torque meter and a magnetic powder brake. The detailed information of the magnetic powder brake and IPMSM is listed in Table 1. A TMS320F28075 32-bit DSP with 120 MHz is adopted in this study to develop the DSP-based servo drive system. Moreover, a torque meter with 100 Nm/7000 rpm is utilized to measure the load torque. The resolution of the adopted encoder is 2500 pulses/rotation and multiplied by 4 by the DSP. The maximum speed of the IPMSM in the experimentation is 4000 rpm in the constant power region. Therefore, by using the gearbox with a gear ratio of 4:1 to reduce the speed, the resulted maximum speed 1000 rpm is smaller than the rated speed of the magnetic powder brake 1800 rpm. Furthermore, the ratings of the adopted CCVSI is 5 kW/220 V/14 A. The switching frequency 10 kHz is controlled by the SVPWM technology. In addition, the dc-link voltage provided by an adjustable DC power supply is set at 311 V. According to the SVPWM, the inverter maximum phase voltage V_{s_max} was set to be $311/\sqrt{3} \approx 179$V. In general, the bandwidth of the current and voltage control loops is 10 times of the speed control loop. Additionally, the operation cycles and execution time of the WFNN estimator is 12261 cycles/102.175 μs. Though the proposed WFNN estimator is more complicated, the execution time is still within 1 ms. Thus, the sampling time of the speed, current, voltage control loops are 1 ms, 0.1 ms, 0.1 ms, respectively.

The experimental results are presented to verify the effectiveness of the designed voltage control for the operating speed above the rated speed. The parameters of the proposed ABNC are given as follows:

$$c_1 = 6.25, \quad c_2 = 5.5, \quad \delta = 130 \quad (47)$$

Moreover, the parameters of the PI controller of the proposed voltage angle controller are given as $K_P = 0.04$ and $K_I = 5$ where K_P and K_I represent the proportional and integral gains. These parameters are tuned by trial and error to achieve the best response. Furthermore, to demonstrate the wide speed control range of the proposed voltage control scheme, the torque-speed curve with four experimental cases are presented in Fig. 7. The first case is the operating condition with rated speed 2000 rpm and rated torque 9.5 Nm. In addition, three operating conditions transforming from the current control mode to the voltage control mode to achieve

the constant power control at rated output power 2kW, which are 3500 rpm under 5.43 Nm load torque, 3750 rpm under 5.07 Nm load torque and 4000 rpm under 4.75 Nm load torque, are tested.

For the comparison of the control performance, the experimental results of PI speed controller with proportional gain 2 and integral gain 0.14 are also given. The gains of the PI speed controller are obtained by trial and error to achieve acceptable transient and steady-state responses. To demonstrate the control performance of the PI and ABNC speed controllers, the IPMSM is operated at rated speed 2000 rpm and rated torque 9.5 Nm with 100 rpm step command, and the results are shown in Fig. 8. Figs. 8(a) and 8(b) present the mechanical speed command ω_{rm}^*, the mechanical speed ω_{rm} and the mechanical speed error e_1. Figs. 8(c) and 8(d) present the q-axis current command i_q^*, q-axis current i_q, d-axis current command i_d^* and d-axis current i_d. The stator voltage command v_s^*, the q-axis voltage command v_q^* and the d-axis voltage command v_d^* are shown in Figs. 8(e) and 8(f). In Fig. 8, since the stator voltage command is less than the maximum phase voltage ($V_{s\_max} \approx 179$V) of the CCVSI, the
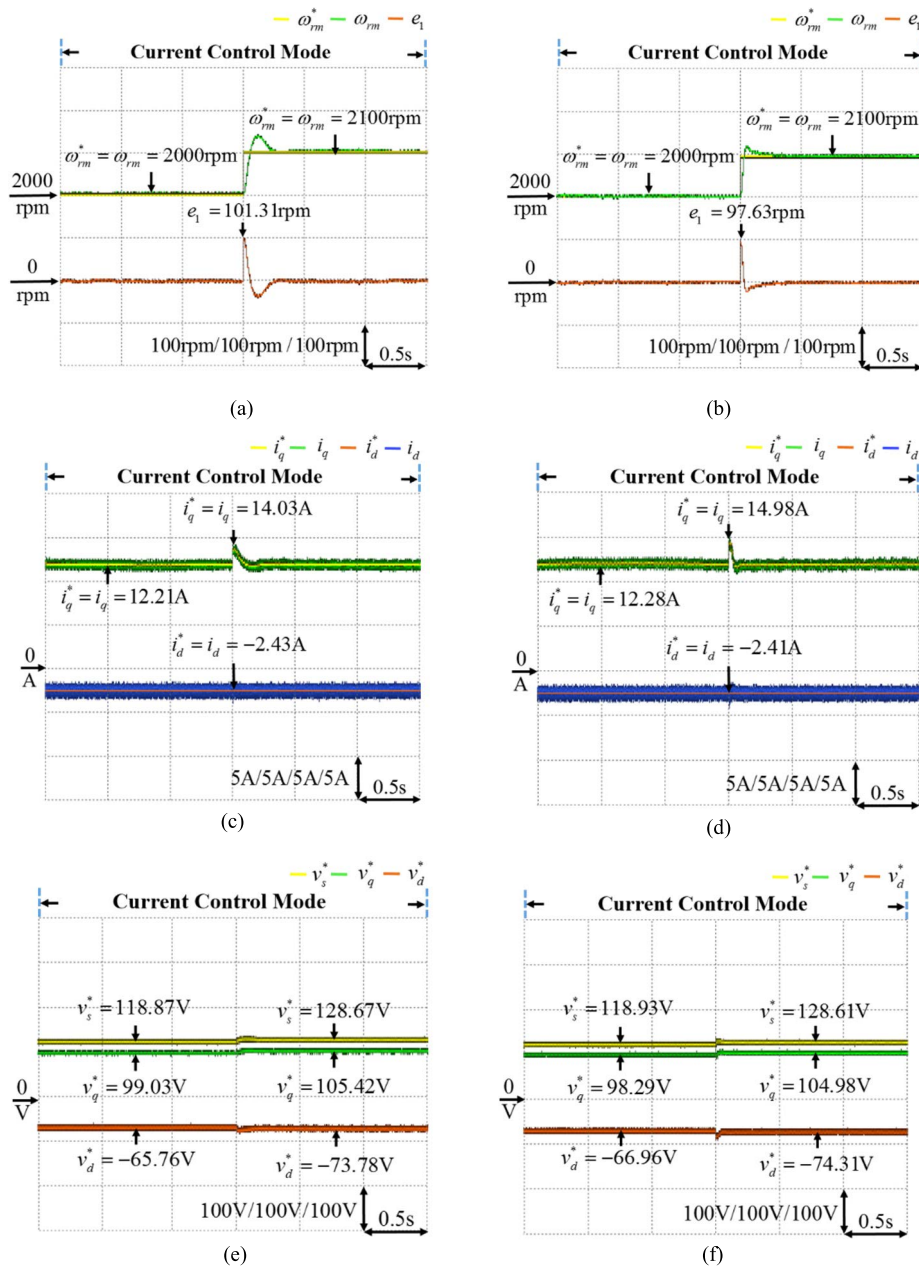
FIGURE 8. Experimental results of PI and ABNC with step command at 2000rpm with 9.5Nm. (a) Mechanical speed command, mechanical speed, mechanical speed error of PI. (b) Mechanical speed command, mechanical speed, mechanical speed error of ABNC. (c) *q*-axis current command, *q*-axis current, *d*-axis current command, *d*-axis current of PI. (d) *q*-axis current command, *q*-axis current, *d*-axis current command, *d*-axis current of ABNC. (e) Stator voltage command, *q*-axis voltage command, *d*-axis voltage command of PI. (f) Stator voltage command, *q*-axis voltage command, *d*-axis voltage command of ABNC.

switching signal of the mode selector remains at the current control mode with MTPA control shown in (26). Moreover, it can be seen from Figs. 8(a) and 8(b) that the overshoot of the PI speed controller is 31.8%, and the overshoot of the ABNC speed controller is 13.3%. Furthermore, the peak value of speed tracking error of PI and ABNC are 101.31 rpm and 97.63 rpm, respectively. In addition, the speed tracking error of PI and ABNC converge to zero in 0.31 sec and 0.24

sec, respectively. Therefore, comparing with the PI speed controller, the ABNC speed controller possesses more robust control characteristic.

Figs. 9-11 depict the experimental resulted of the current and voltage control for the mechanical speed command increasing from 2000 rpm to 3500 rpm under 5.43 Nm load torque, 2000 rpm to 3750 rpm under 5.07 Nm load torque, and 2000 rpm to 4000 rpm under 4.75 Nm load torque,
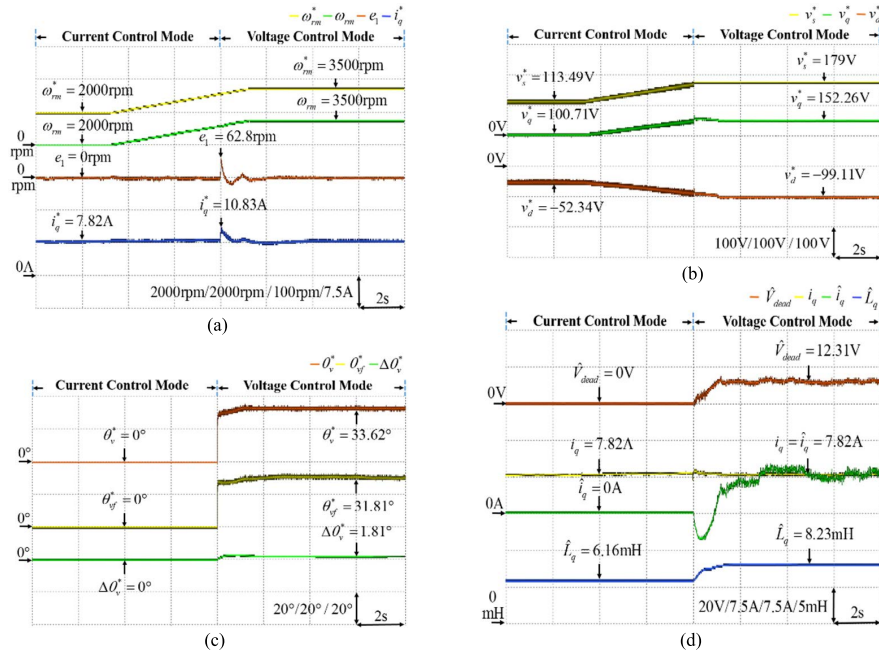
FIGURE 9. Experimental results of current and voltage control from 2000rpm to 3500rpm under 5.43Nm load torque. (a) Mechanical speed command, mechanical speed, mechanical speed error, *q*-axis current command. (b) Stator voltage command, *q*-axis voltage command, *d*-axis voltage command. (c) Voltage angle command, feedforward voltage angle command, compensating voltage angle command. (d) Estimated distorted voltage, *q*-axis current, estimated *q*-axis current, estimated *q*-axis inductance.
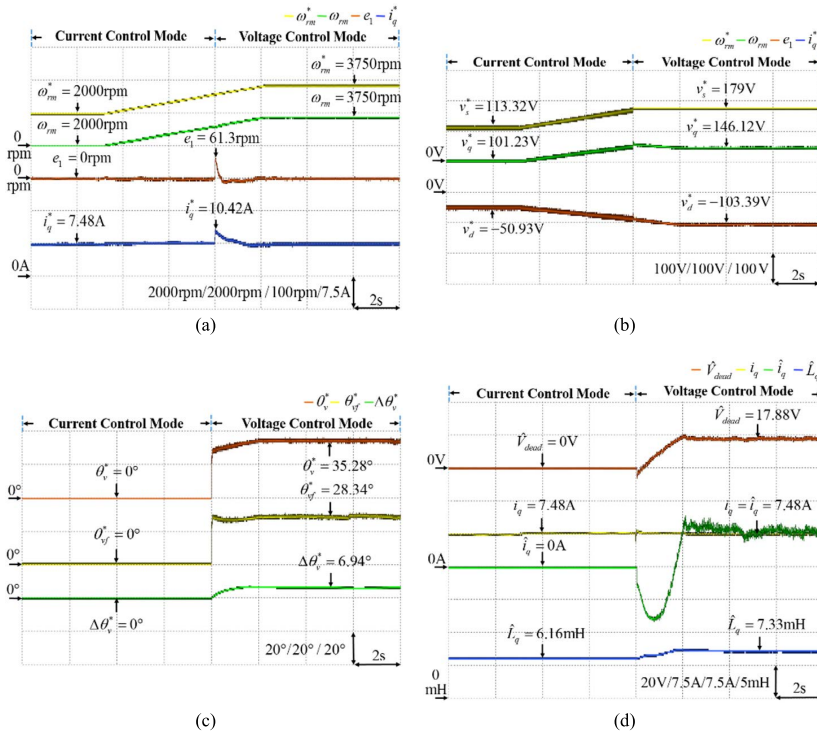

FIGURE 10. Experimental results of current and voltage control from 2000rpm to 3750rpm under 5.07Nm load torque. (a) Mechanical speed command, mechanical speed, mechanical speed error, *q*-axis current command. (b) Stator voltage command, *q*-axis voltage command, *d*-axis voltage command. (c) Voltage angle command, feedforward voltage angle command, compensating voltage angle command. (d) Estimated distorted voltage, *q*-axis current, estimated *q*-axis current, estimated *q*-axis inductance.

respectively. Figs. 9(a), 10(a), 11(a) present the mechanical speed command ω_{rm}^*, the mechanical speed ω_{rm}, the

mechanical speed error e_1 and the q-axis current command i_q^*. Figs. 9(b), 10(b), 11(b) depict the stator voltage command
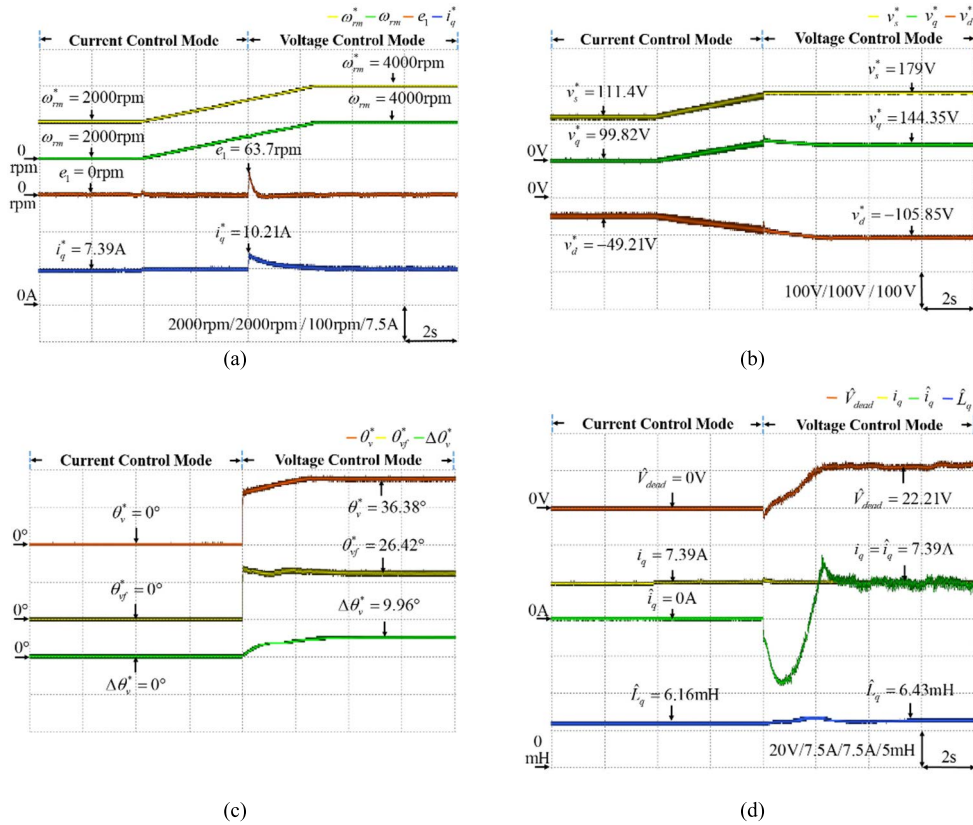
FIGURE 11. Experimental results of current and voltage control from 2000rpm to 4000rpm under 4.75Nm load torque. (a) Mechanical speed command, mechanical speed, mechanical speed error, q-axis current command. (b) Stator voltage command, q-axis voltage command, d-axis voltage command. (c) Voltage angle command, feedforward voltage angle command, compensating voltage angle command. (d) Estimated distorted voltage, q-axis current, estimated q-axis current, estimated q-axis inductance.

v_s^*, the q-axis voltage command v_q^* and the d-axis voltage command v_d^*. Figs. 9(c), 10(c), 11(c) show the voltage angle command θ_v^*, the feedforward voltage angle command θ_{vf}^* and the compensating voltage angle command $\Delta\theta_v^*$. The estimated distortion voltage $\hat{V}_{dead}$, the q-axis current i_q, the estimated q-axis current $\hat{i}_q$, and the estimated q-axis inductance $\hat{L}_q$ are shown in Figs. 9(d), 10(d), 11(d) by using the scheme shown in Fig. 5. From the experimental results shown in Figs. 9-11, once the stator voltage command v_s^* reaches the maximum phase voltage V_{s_max} of the inverter, the switch signal of the mode selector will transit to the voltage control mode from the current control mode. During the transition, due to the robust control characteristic of the ABNC, the speed error converges immediately. Moreover, when the motor operates at rated speed with different load conditions, the operating points are located at the intersections of torque trajectories and MTPA curve. Above the rated speed, the voltage limit ellipse will shrink with the increasing speed. Then, the operating points will move to the intersections of torque trajectories and the voltage limit ellipses. According to Fig. 1, the higher the operating speed, the more the negative value of d-axis current i_d is at the same load condition. The above situation will result in higher voltage angle command θ_v^* and more negative value of d-axis voltage command v_d^* as shown in Figs. 9(b), 10(b), 11(b) and 9(c), 10(c), 11(c). Furthermore, the estimated distortion voltage $\hat{V}_{dead}$ can be obtained by using Eq. (43), which is larger at higher speed with lower torque as shown in Figs. 9(d), 10(d), 11(d). The same phenomenon can also be found in [18]. In addition, the estimated $\hat{L}_q$ are 8.23mH, 7.33mH and 6.43mH, respectively, by using the proposed intelligent q-axis inductance estimation scheme at three FW operating conditions as shown in Figs. 9(d), 10(d), 11(d). The estimated value of the q-axis inductance decreases with higher voltage angle at higher speed. The above result has also been obtained in both [6] and [27]. Additionally, the successful model following dynamics of the estimated voltage model of the IPMSM servo drive and the voltage model of the IPMSM servo drive by the tracking of the estimated q-axis current $\hat{i}_q$ to the q-axis current i_q also can be found in Figs. 9(d), 10(d), 11(d). Therefore, the voltage control with rated output power could be achieved at high speed by using the proposed voltage control scheme.

For the comparison of control performance of the q-axis inductance $\hat{L}_q$ estimation scheme, the WFNN shown in Fig. 5 is replaced by a traditional PI estimation method. Figs. 12(a) and 12(b), Figs. 12(c) and 12(d), and
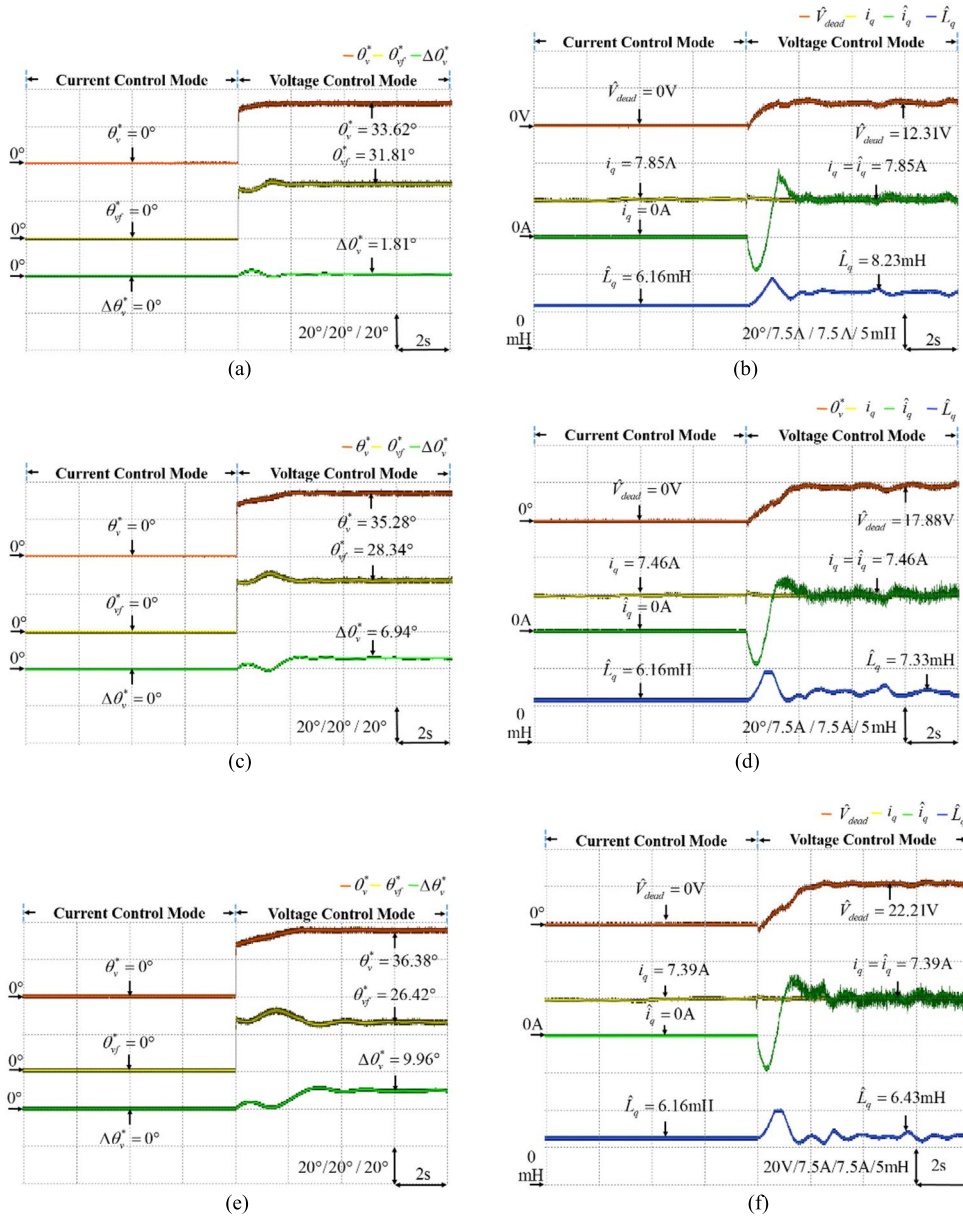
FIGURE 12. Experimental results of current and voltage control using PI estimation. (a) Voltage angle command, feedforward voltage angle command, compensating voltage angle command from 2000rpm to 3500rpm under 5.43Nm load torque. (b) Estimated distorted voltage, *q*-axis current, estimated *q*-axis current, estimated *q*-axis inductance from 2000rpm to 3500rpm under 5.43Nm load torque. (c) Voltage angle command, feedforward voltage angle command, compensating voltage angle command from 2000rpm to 3750rpm under 5.07Nm load torque. (d) Estimated distorted voltage, *q*-axis current, estimated *q*-axis current, estimated *q*-axis inductance from 2000rpm to 3750rpm under 5.07Nm load torque. (e) Voltage angle command, feedforward voltage angle command, compensating voltage angle command from 2000rpm to 4000rpm under 4.75Nm load torque. (f) Estimated distorted voltage, *q*-axis current, estimated *q*-axis current, estimated *q*-axis inductance from 2000rpm to 4000rpm under 4.75Nm load torque.

Figs. 12(e) and 12(f) depict the experimental results of the current and voltage control for the mechanical speed command increasing from 2000 rpm to 3500 rpm under 5.43 Nm load torque, 2000 rpm to 3750 rpm under 5.07 Nm load torque, and 2000 rpm to 4000 rpm under 4.75 Nm load torque, respectively, by using the PI parameter estimation scheme. Figs. 12(a), 12(c) and 12(e) show the voltage angle command θ_v^*, the feedforward voltage angle command θ_{vf}^* and the compensating voltage angle command $\Delta\theta_v^*$. Moreover, the estimated distortion voltage $\hat{V}_{dead}$, the *q*-axis current i_q, the estimated *q*-axis current $\hat{i}_q$, and the estimated *q*-axis inductance $\hat{L}_q$ are also 8.23mH, 7.33mH and 6.43mH as shown in Figs. 12(b), 12(d) and 12(f). Though the estimated steady-state values of $\hat{L}_q$ by using PI estimation scheme at

three FW operating conditions are the same as the WFNN estimation scheme shown in Figs. 9(d), 10(d) and 11(d), the sluggish response of the PI parameter estimation scheme obstructs its usefulness in practical applications.

Comparing with the real-time torque control and online stator flux estimation method developed in [12], an ABNC speed controller considering nonzero d-axis current was proposed in this study to improve the robustness of the speed control. Moreover, a feedforward voltage angle controller, in which an intelligent parameter estimation method using WFNN is adopted to estimate the q-axis inductance online, was successfully developed for the speed control in the constant power region. On the other hand, the estimation model shown in (33) and (34) ignores the influence of stator resistance. If it is considered, the estimation accuracy can be improved. Besides, the operation cycles and execution time of the WFNN estimator is 12261 cycles/102.175 μs. Though the execution time is still within 1 ms sampling time of the speed control loop, the proposed WFNN estimator is rather complicated. A simplified FNN model will be considered in the future to reduce the calculation burden of the DSP.

VI. CONCLUSION

A novel voltage control scheme using a feedforward voltage angle controller with online intelligent parameter estimation method for the q-axis inductance was successfully developed for an IPMSM servo drive in this study. First, an ABNC speed controller was developed to improve the transient response of the speed control. Then, the MTPA method is used in the current control mode for the constant torque region. Moreover, the feedforward voltage angle controller with intelligent parameter estimation using WFNN was designed to improve the dynamic response in the voltage control mode for the constant power region. Furthermore, the q-axis current controller was retained to ensure the steady-state response. In addition, the experimental results of three operating conditions transforming from the current control mode to the voltage control mode to achieve the constant power control at rated output power were provided to demonstrate the validity of the proposed control methods of the IPMSM servo drive system.

REFERENCES

[1] E.-K. Kim, J. Kim, H. H. Choi, and J.-W. Jung, "Variable structure speed controller guaranteeing robust transient performance of an IPMSM drive," *IEEE Trans. Ind. Informat.*, vol. 15, no. 6, pp. 3300–3310, Jun. 2019.

[2] B. A. Basit, H. H. Choi, and J.-W. Jung, "An online torque ripple minimization technique for IPMSM drives: Fuzzy system-based d-axis current design approach," *IEEE Trans. Ind. Electron.*, vol. 68, no. 12, pp. 11794–11805, Dec. 2021.

[3] M. Fasil, C. Antaloae, N. Mijatovic, B. B. Jensen, and J. Holboll, "Improved *dq*-axes model of PMSM considering airgap flux harmonics and saturation," *IEEE Trans. Appl. Supercond.*, vol. 26, no. 4, pp. 1–5, Jun. 2016.

[4] F.-J. Lin, Y.-H. Liao, J.-R. Lin, and W.-T. Lin, "Interior permanent magnet synchronous motor drive system with machine learning-based maximum torque per ampere and flux-weakening control," *Energies*, vol. 14, no. 2, p. 346, Jan. 2021.

[5] J.-M. Kim and S.-K. Sul, "Speed control of interior permanent magnet synchronous motor drive for the flux weakening operation," *IEEE Trans. Ind. Appl.*, vol. 33, no. 1, pp. 43–48, Jan./Feb. 1997.

[6] Y. Chen, X. Huang, J. Wang, F. Niu, J. Zhang, Y. Fang, and L. Wu, "Improved flux-weakening control of IPMSMs based on torque feed-forward technique," *IEEE Trans. Power Electron.*, vol. 33, no. 12, pp. 10970–10978, Dec. 2018.

[7] M. Huang, K. Chen, C. Chen, Z. Li, and S. Hung, "Torque control in constant power region for IPMSM under six-step voltage operation," *IET Electr. Power Appl.*, vol. 13, no. 2, pp. 181–189, Feb. 2019.

[8] D. Stojan, D. Drevensek, Z. Plantic, B. Grcar, and G. Stumberger, "Novel field-weakening control scheme for permanent-magnet synchronous machines based on voltage angle control," *IEEE Trans. Ind. Appl.*, vol. 48, no. 6, pp. 2390–2401, Nov./Dec. 2012.

[9] Y. Zhang, L. Xu, M. K. Güven, S. Chi, and M. Illindala, "Experimental verification of deep field weakening operation of a 50-kW IPM machine by using single current regulator," *IEEE Trans. Ind. Appl.*, vol. 47, no. 1, pp. 128–133, Jan./Feb. 2011.

[10] Z. Zhang, C. Wang, M. Zhou, and X. You, "Flux-weakening in PMSM drives: Analysis of voltage angle control and the single current controller design," *IEEE J. Emerg. Sel. Topics Power Electron.*, vol. 7, no. 1, pp. 437–445, Mar. 2019.

[11] T. Miyajima, H. Fujimoto, and M. Fujitsuna, "A precise model-based design of voltage phase controller for IPMSM," *IEEE Trans. Power Electron.*, vol. 28, no. 12, pp. 5655–5664, Dec. 2013.

[12] H.-S. Kim and S.-K. Sul, "Real-time torque control of IPMSM under flux variations," *IEEE J. Emerg. Sel. Topics Power Electron.*, vol. 10, no. 3, pp. 3345–3356, Jun. 2022.

[13] D. Q. Dang, M. S. Rafaq, H. H. Choi, and J.-W. Jung, "Online parameter estimation technique for adaptive control applications of interior PM synchronous motor drives," *IEEE Trans. Ind. Electron.*, vol. 63, no. 3, pp. 1438–1449, Mar. 2016.

[14] F. Erturk and B. Akin, "Spatial inductance estimation for current loop auto-tuning in IPMSM self-commissioning," *IEEE Trans. Ind. Electron.*, vol. 67, no. 5, pp. 3911–3920, May 2020.

[15] M. X. Bui, M. F. Rahman, D. Guan, and D. Xiao, "A new and fast method for on-line estimation of d and q axes inductances of interior permanent magnet synchronous machines using measurements of current derivatives and inverter DC-bus voltage," *IEEE Trans. Ind. Electron.*, vol. 66, no. 10, pp. 7488–7497, Oct. 2019.

[16] M. N. Uddin and M. M. I. Chy, "Online parameter-estimation-based speed control of PM AC motor drive in flux-weakening region," *IEEE Trans. Ind. Appl.*, vol. 44, no. 5, pp. 1486–1494, Sep. 2008.

[17] K. Liu and Z. Q. Zhu, "Position-offset-based parameter estimation using the adaline NN for condition monitoring of permanent-magnet synchronous machines," *IEEE Trans. Ind. Electron.*, vol. 62, no. 4, pp. 2372–2383, Apr. 2015.

[18] F.-J. Lin, S.-Y. Chen, W.-T. Lin, and C.-W. Liu, "An online parameter estimation using current injection with intelligent current-loop control for IPMSM drives," *Energies*, vol. 14, no. 23, p. 8138, Dec. 2021.

[19] D. Zhao, W. Chen, J. Wu, and J. Li, "Globally stable adaptive tracking control for uncertain strict-feedback systems based on neural network approximation," *Asian J. Control*, vol. 18, no. 1, pp. 1–12, 2016.

[20] F.-J. Lin, M.-S. Huang, S.-G. Chen, C.-W. Hsu, and C.-H. Liang, "Adaptive backstepping control for synchronous reluctance motor based on intelligent current angle control," *IEEE Trans. Power Electron.*, vol. 35, no. 7, pp. 7465–7479, Jul. 2020.

[21] F.-J. Lin, S.-G. Chen, and I.-F. Sun, "Adaptive backstepping control of six-phase PMSM using functional link radial basis function network uncertainty observer," *Asian J. Control*, vol. 19, no. 6, pp. 2255–2269, Nov. 2017.

[22] T. Li, X. Liu, and H. Yu, "Backstepping nonsingular terminal sliding mode control for PMSM with finite-time disturbance observer," *IEEE Access*, vol. 9, pp. 135496–135507, 2021.

[23] Y. Zhao, X. Sun, G. Wang, and Y. Fan, "Adaptive backstepping sliding mode tracking control for underactuated unmanned surface vehicle with disturbances and input saturation," *IEEE Access*, vol. 9, pp. 1304–1312, 2021.

[24] S. Yilmaz and Y. Oysal, "Fuzzy wavelet neural network models for prediction and identification of dynamical systems," *IEEE Trans. Neural Netw.*, vol. 21, no. 10, pp. 1599–1609, Oct. 2010.

[25] F.-J. Lin, Y.-T. Liu, and W.-A. Yu, "Power perturbation based MTPA with an online tuning speed controller for an IPMSM drive system," *IEEE Trans. Ind. Electron.*, vol. 65, no. 5, pp. 3677–3687, May 2018.

[26] F.-J. Lin, Y.-C. Hung, and K.-C. Ruan, "An intelligent second-order sliding-mode control for an electric power steering system using a wavelet fuzzy neural network," *IEEE Trans. Fuzzy Syst.*, vol. 22, no. 6, pp. 1598–1611, Dec. 2014.

[27] B. H. Lee, S. O. Kwon, T. Sun, J. P. Hong, G. H. Lee, and J. Hur, "Modeling of core loss resistance for $d-q$ equivalent circuit analysis of IPMSM considering harmonic linkage flux," *IEEE Trans. Magn.*, vol. 47, no. 5, pp. 1066–1069, May 2011.

CHIH-WEI LIU was born in Kaohsiung, Taiwan, in 1997. He received the B.S. degree in electrical engineering from the National Yunlin University of Science and Technology, Yunlin, Taiwan, in 2020. He is currently pursuing the M.S. degree in electrical engineering with National Central University, Chungli, Taiwan. His research interests include DSP-based control systems, motor servo drive systems, and intelligent control theories.

FAA-JENG LIN (Fellow, IEEE) received the B.S. and M.S. degrees in electrical engineering from National Cheng Kung University, Taiwan, in 1983 and 1985, respectively, and the Ph.D. degree in electrical engineering from National Tsing Hua University, Taiwan, in 1993. Currently, he is a Chair Professor with the Department of Electrical Engineering, National Central University, Taiwan. His research interests include AC motor drives, power electronics, renewable energies, smart grids, intelligent and nonlinear control theories. His work has been widely cited. Several of his papers have helped to establish research areas, such as fuzzy neural network control of motor drives and motion control systems, and resonant converters for piezo-ceramic motor drives. He was the President of Taiwan Smart Grid Industry Association from 2012 to 2016. He is a fellow of IET. He is the Executive Director of Taiwan Power Company. He received the Outstanding Research Awards from the National Science Council, Taiwan, in 2004, 2010, and 2013; and the Outstanding Professor of Engineering Award in 2016 from the Chinese Institute of Engineers, Taiwan. He was the Chair and Principle Investigator of the Smart Grid Focus Center, National Energy Project Phase I and II in Taiwan, from 2011 to 2019. He was an Associate Editor of IEEE TRANSACTIONS ON FUZZY SYSTEMS. He is currently an Associate Editor of IEEE TRANSACTIONS ON POWER ELECTRONICS.

PO-LUN WANG was born in New Taipei, Taiwan, in 1998. He received the B.S. degree in mechanical engineering from National Central University, Chungli, Taiwan, in 2021, where he is currently pursuing the M.S. degree in electrical engineering. His research interests include DSP-based control systems, motor servo drive systems, and intelligent control theories.

• • •